



Measurements of long-range near-side angular correlations in $\sqrt{s_{NN}} = 5$ TeV proton-lead collisions in the forward region

The LHCb Collaboration



ARTICLE INFO

Article history:

Received 10 December 2015

Received in revised form 27 September 2016

Accepted 30 September 2016

Available online 6 October 2016

Editor: W.-D. Schlatter

ABSTRACT

Two-particle angular correlations are studied in proton-lead collisions at a nucleon–nucleon centre-of-mass energy of $\sqrt{s_{NN}} = 5$ TeV, collected with the LHCb detector at the LHC. The analysis is based on data recorded in two beam configurations, in which either the direction of the proton or that of the lead ion is analysed. The correlations are measured in the laboratory system as a function of relative pseudorapidity, $\Delta\eta$, and relative azimuthal angle, $\Delta\phi$, for events in different classes of event activity and for different bins of particle transverse momentum. In high-activity events a long-range correlation on the near side, $\Delta\phi \approx 0$, is observed in the pseudorapidity range $2.0 < \eta < 4.9$. This measurement of long-range correlations on the near side in proton-lead collisions extends previous observations into the forward region up to $\eta = 4.9$. The correlation increases with growing event activity and is found to be more pronounced in the direction of the lead beam. However, the correlation in the direction of the lead and proton beams are found to be compatible when comparing events with similar absolute activity in the direction analysed.

© 2016 The Author. Published by Elsevier B.V. This is an open access article under the CC BY license (<http://creativecommons.org/licenses/by/4.0/>). Funded by SCOAP³.

1. Introduction

Studies of two-particle angular correlations are an important experimental method to investigate the dynamics of multi-particle production in QCD and to probe collective effects arising in the dense environment of a high-energy collision. The highest particle densities and multiplicities reached in proton–proton (pp) and proton-lead collisions (pPb) at the LHC are of a similar size to those in non-central nucleus–nucleus (AA) collisions. This motivates looking for signatures which were so far mainly studied in AA collisions.

Two-particle correlations are conveniently described by two-dimensional $(\Delta\eta, \Delta\phi)$ -correlation functions. For pairs of prompt charged particles their separations in pseudorapidity, $\Delta\eta$, and in the azimuthal angle, $\Delta\phi$, are measured in the laboratory system. Structures in the correlation function are classified into short-range ($|\Delta\eta| \lesssim 2$) and long-range ($|\Delta\eta| \gtrsim 2$) effects. On the near-side ($|\Delta\phi| \approx 0$) a short-range “jet peak” at $\Delta\eta \approx 0$ is the dominant structure, caused by the fact that in the fragmentation process the final-state particles are collimated around the initial parton. To balance the momentum, the peak is accompanied by a long-range structure on the away side ($|\Delta\phi| \approx \pi$) caused by particles that are opposite in azimuthal angle.

Due to the different momentum fractions carried by the colliding partons and the resulting individual boosts, the away-side structure is not restricted in $\Delta\eta$, but elongated over a large range. In complex heavy-ion collisions, these short- and long-range struc-

tures are modified as a result of the strongly interacting medium that is formed depending on the centrality of the collision. Long-range correlations on the near- and away-side are observed, which are typically explained as being the result of a hydrodynamical flow of the deconfined medium [1]. Measurements in very rare pp collisions that have an extremely high particle multiplicity revealed a similar unexpected long-range correlation on the near side [2–4]. This structure, often referred to as the near-side “ridge”, has also been confirmed in high-multiplicity pPb collisions [5–9], where it was found to be much more pronounced than in pp collisions.

The theoretical interpretation of the mechanism responsible for the ridge in pp and pPb is still under discussion. Various models have been proposed such as gluon saturation in the framework of a colour-glass condensate [10–13] or the hydrodynamic evolution of a high density partonic medium [14], multiparton interactions [15–17], jet-medium interactions [18,19], and collective effects [20–24] induced by the formation and expansion of a high-density system possibly produced in these collisions. Analyses that have seen the near-side ridge at the LHC have been performed in the central rapidity region, probing ranges up to $|\eta| = 2.5$. In a recent analysis [9] larger pseudorapidities were also accessed in measurements of muon–hadron correlations between the forward ($2.5 < |\eta| < 4.0$) and the central ($|\eta| < 1.0$) region. For the present measurement the forward acceptance of the LHCb detector, unique among the LHC experiments, is used to study the ridge phenomenon in pPb collisions. Proton-lead collisions are analysed in the range of $2.0 < \eta < 4.9$ and in the directions of the proton

and the lead beams separately. Confirmation of the ridge correlation at large pseudorapidities and comparison of its magnitude for the two beam directions provide new input to the theoretical understanding of the underlying mechanisms.

2. Experimental setup

The analysis is based on data collected with the LHCb detector during the proton-lead data-taking period in 2013. The LHC provided p Pb collisions at a nucleon–nucleon centre-of-mass energy of $\sqrt{s_{NN}} = 5$ TeV, corresponding to a proton beam energy of 4 TeV and a lead beam energy of 1.58 TeV per nucleon. Due to this asymmetric beam configuration, there is a relative boost between the rapidity in the LHCb laboratory frame, y_{lab} , and y in the nucleon–nucleon centre-of-mass frame, corresponding to a shift of 0.47 units.

The LHCb detector [25,26] is a single-arm forward spectrometer covering the pseudorapidity range $2 < \eta < 5$ in the laboratory frame. Depending on the direction of the proton and the lead beam, two different configurations are distinguished. In the *forward* configuration the proton beam points to positive rapidity, into the LHCb spectrometer, and the recorded collisions are referred to as $p + \text{Pb}$. The opposite *backward* configuration, in which the lead beam points to positive rapidity, is referred to as $\text{Pb} + p$. The measurement is performed in the LHCb laboratory frame, probing rapidities y in the nucleon–nucleon centre-of-mass frame of $1.5 < y < 4.4$ in the $p + \text{Pb}$ configuration and $-5.4 < y < -2.5$ in the $\text{Pb} + p$ configuration. The data used for this analysis correspond to an integrated luminosity of 0.46 nb^{-1} in the $p + \text{Pb}$ configuration and 0.30 nb^{-1} for the $\text{Pb} + p$ configuration.

The LHCb detector, designed for the study of particles containing b or c quarks, includes a high-precision tracking system consisting of a silicon-strip vertex detector (VELO) surrounding the interaction region, a large-area silicon-strip detector located upstream of a dipole magnet with a bending power of about 4 Tm, and three stations of silicon-strip detectors and straw drift tubes placed downstream of the magnet. The polarity of the dipole magnet was reversed once for each configuration to average over small asymmetries in the detection of charged particles. The tracking system provides a measurement of momentum of charged particles with a relative uncertainty that varies from 0.5% at low momentum to 1.0% at 200 GeV/c. Different types of charged hadrons are distinguished using information from two ring-imaging Cherenkov detectors. Photons, electrons and hadrons are identified by a calorimeter system consisting of scintillating-pad and preshower detectors, an electromagnetic calorimeter and a hadronic calorimeter. Muons are identified by a system composed of alternating layers of iron and multiwire proportional chambers. The online event selection is performed by a trigger, which consists of a hardware stage, based on information from the calorimeter and muon systems, followed by a software stage, which applies a full event reconstruction. During data taking of p Pb collisions, an activity trigger in the hardware stage accepted non-empty beam bunch crossings, and the software stage accepted events with at least one reconstructed track in the VELO.

3. Data selection and corrections

Monte Carlo simulations are used to evaluate the efficiency of the following selections and to estimate the remaining contamination in the selected track sample. Proton-lead collisions in $p + \text{Pb}$ and $\text{Pb} + p$ configurations are simulated using the HIJING generator [27] in version 1.383bs.2. As a cross-check, proton–proton collisions at a centre-of-mass energy of 8 TeV are simulated using PYTHIA [28] in a special LHCb configuration [29] and with a

high average interaction rate (large pile-up) to reproduce the larger particle multiplicity in proton-lead collisions. Particle decays are simulated by EVTGEN [30]. The interaction of the generated particles with the detector, and its response, are implemented using the GEANT4 toolkit [31] as described in Ref. [32].

The measurements are based on proton-lead collisions that are dominated by single interactions; fewer than 2% of the bunch crossings have more than one interaction. Each event is required to have exactly one reconstructed primary vertex containing at least five tracks. Beam-related background interactions are suppressed by requiring the position of the reconstructed primary vertex to be within ± 3 standard deviations around the mean interaction point, separately for each coordinate. The mean value and the width of this luminous region are determined separately from a Gaussian fit to the distribution of reconstructed primary vertices of each data sample. Depending on the polarity of the magnetic field and the resulting beam optics, the size of the standard deviation along the beam axis is approximately 40 mm or 60 mm, while in the transverse direction it is around 30 μm . While p Pb interactions are most likely produced in this region, beam-related background extends further along the beam line. Beam gas events or interactions with detector material can produce a very high number of particles; however, in such cases the total energy deposit in the calorimeter is much smaller than that of typical p Pb collisions. Events with too small a ratio of the number of clusters in the electromagnetic calorimeter to that in the VELO are rejected; individual lower bounds are defined for collisions in the $p + \text{Pb}$ and $\text{Pb} + p$ configuration using simulation.

The angular correlations are determined for charged particles that are directly produced in the p Pb interaction. The measurement is based on tracks traversing the full tracking system, which restricts charged particles in pseudorapidity to $2.0 < \eta < 4.9$. In addition, particles are required to have a transverse momentum $p_T > 0.15$ GeV/c and a total momentum $p > 2$ GeV/c. Reconstruction artefacts, such as fake tracks, are suppressed using a multivariate classifier. The remaining average fraction of fake tracks is of the order of 7% and 12% in the $p + \text{Pb}$ and $\text{Pb} + p$ samples, respectively. The probability of reconstructing fake tracks increases with the number of hits in the tracking detectors. Thus, the difference between the data samples is due to the higher average particle and hit multiplicity that is present in the direction of the lead remnant. To select primary tracks originating directly from the p Pb collision the impact parameter of each track with respect to the reconstructed primary vertex must not exceed 1.2 mm, after which the fraction of remaining tracks from secondary particles is estimated to be less than 3.5%.

The inefficiency in finding charged particles arises from two effects: limited detector acceptance in the range of $2.0 < \eta < 4.9$, and limitations of the track reconstruction. For particles fulfilling the kinematic requirements, the acceptance describes the fraction that reach the end of the downstream tracking stations and is about 70% on average. In contrast, the track reconstruction efficiency varies from 96% for low-multiplicity events to 60% for events with the highest measured multiplicity.

After applying the selection requirements, the remaining probabilities of selecting fake tracks, $\mathcal{P}_{\text{fake}}$, and secondary particles, \mathcal{P}_{sec} , as well as the efficiencies related to the detector acceptance, ϵ_{acc} , and the track reconstruction, ϵ_{tr} , are estimated in simulation as a function of the angular variables η and ϕ , the transverse momentum p_T , and the hit-multiplicity in the VELO, $\mathcal{N}_{\text{VELO}}^{\text{hit}}$. Each reconstructed track is assigned a weight, ω , that accounts for these effects:

$$\omega(\eta, \phi, p_T, \mathcal{N}_{\text{VELO}}^{\text{hit}}) = (1 - \mathcal{P}_{\text{fake}} - \mathcal{P}_{\text{sec}}) / (\epsilon_{\text{acc}} \cdot \epsilon_{\text{tr}}). \quad (1)$$

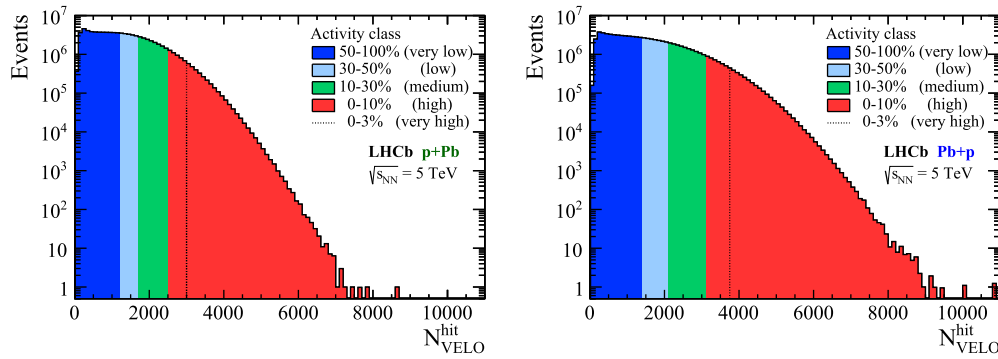


Fig. 1. Hit-multiplicity distribution in the VELO for selected events of the minimum-bias samples in the (left) $p + \text{Pb}$ and (right) $\text{Pb} + p$ configurations. The activity classes are defined as fractions of the full distribution, as indicated by colours (shades). The 0–3% class is a sub-sample of the 0–10% class. (For interpretation of the references to colour in this figure legend, the reader is referred to the web version of this article.)

Table 1

Relative event-activity classes defined by the VELO-hit multiplicity, $\mathcal{N}_{\text{VELO}}^{\text{hit}}$, of an event. The classes are defined as fractions of the $\mathcal{N}_{\text{VELO}}^{\text{hit}}$ distribution for minimum-bias recorded events in the $p + \text{Pb}$ or $\text{Pb} + p$ configuration. The 0–3% class is a sub-sample of the 0–10% class. For illustration purposes the average number, $\langle N_{ch} \rangle_{\text{MC}}$, of prompt charged particles with $p > 2 \text{ GeV}/c$, $p_T > 0.15 \text{ GeV}/c$ and $2.0 < \eta < 4.9$ is listed for events simulated with the HIJING event generator. Statistical uncertainties are negligible.

Relative activity class	$p + \text{Pb}$		$\text{Pb} + p$	
	Range $\mathcal{N}_{\text{VELO}}^{\text{hit}}$	$\langle N_{ch} \rangle_{\text{MC}}$	Range $\mathcal{N}_{\text{VELO}}^{\text{hit}}$	$\langle N_{ch} \rangle_{\text{MC}}$
50–100% very low	0–1200	18.9	0–1350	29.2
30–50% low	1200–1700	30.0	1350–2000	47.4
10–30% medium	1700–2400	42.8	2000–3000	70.9
0–10% high	2400–max	63.6	3000–max	106.7
0–3% very high	3000–max	73.7	3800–max	126.4

4. Activity classes and data samples

Two-particle correlations show a strong dependence on the number of particles produced within a collision. The hit multiplicity in the VELO is proportional to this global event property. With its coverage in pseudorapidity ranging from $1.9 < \eta < 4.9$ in the forward direction and $-2.5 < \eta < -2.0$ in the backward direction, the VELO can probe the total number of charged particles per event more comprehensively than other sub-detectors of LHCb.

The analysis presented in this paper is based on a subset of the total data set recorded during the 2013 $p\text{Pb}$ running period. The $p + \text{Pb}$ and $\text{Pb} + p$ minimum bias samples each consist of about 1.1×10^8 events which are randomly selected from the about 10 times larger full sample. The high-multiplicity samples contain all recorded events with at least 2200 hits in the VELO and amount to about 1.1×10^8 events in $\text{Pb} + p$ and 1.3×10^8 events in $p + \text{Pb}$ collisions.

Five event-activity classes are defined as fractions of the hit-multiplicity distributions of the minimum-bias samples, as indicated in Fig. 1. Since collisions recorded in the $\text{Pb} + p$ configuration reach larger hit-multiplicities compared to those in the $p + \text{Pb}$ configuration, the relative classes are defined separately for each configuration. The 50–100% class contains approximately the 50% of events with the lowest event activities, followed by the 30–50% and 10–30% classes representing medium-activity events, and the 0–10% and 0–3% classes of high-activity events. The ranges defining the activity classes are listed in Table 1. For each class, average numbers of charged particles, $\langle N_{ch} \rangle_{\text{MC}}$, are quoted for illustration, based on the HIJING event generator.

The long-range correlations in the direction of the fragmenting proton ($p + \text{Pb}$ configuration) and the direction of the fragmenting lead ion ($\text{Pb} + p$ configuration) are compared for classes of the same absolute activity in the pseudorapidity range of $2.0 < \eta <$

Table 2

Common absolute activity bins for the $p + \text{Pb}$ and $\text{Pb} + p$ samples. The activity of $p + \text{Pb}$ events is scaled to match the same activity ranges of $\text{Pb} + p$ events, as explained in the text. For illustration purposes the average number, $\langle N_{ch} \rangle_{\text{MC}}$, of prompt charged particles with $p > 2 \text{ GeV}/c$, $p_T > 0.15 \text{ GeV}/c$ and $2.0 < \eta < 4.9$ is listed for events simulated with the HIJING event generator. The uncertainties are due to the scaling factor of 0.77 ± 0.08 . Statistical uncertainties are negligible.

Common absolute activity bin	$\mathcal{N}_{\text{VELO}}^{\text{hit}}$ -range in $\text{Pb} + p$ scale	$p + \text{Pb}$ $\langle N_{ch} \rangle_{\text{MC}}$	$\text{Pb} + p$ $\langle N_{ch} \rangle_{\text{MC}}$
Bin I	2200–2400	62.8 ± 6.6	64.4
Bin II	2400–2600	68.4 ± 7.1	67.0
Bin III	2600–2800	73.7 ± 7.6	76.4
Bin IV	2800–3000	79.2 ± 7.9	82.4
Bin V	3000–3500	86.7 ± 8.2	92.9

4.9. Here a proper assignment of equivalent activity classes needs to take into account the fact that the VELO acceptance is larger than the pseudorapidity interval of interest. Assuming a linear relation between the total number of VELO hits and the number of tracks in the range $2.0 < \eta < 4.9$, one finds that N VELO hits in the $\text{Pb} + p$ configuration correspond to $N/(0.77 \pm 0.08)$ VELO hits in the $p + \text{Pb}$ case. The uncertainty in the scaling factor accounts for deviations from perfect linearity in the data that are not reproduced in the simulation, and is propagated into the systematic uncertainties of the results. Five common absolute activity classes, labelled I–V, are defined in the high-activity region and are listed in Table 2 with the corresponding average numbers of charged particles from simulation. The quoted uncertainties in the $p + \text{Pb}$ sample are related to the systematic uncertainty of the scaling factor.

The analysis is repeated using an alternative event-activity classification, based on the multiplicity of selected tracks in the range $2.0 < \eta < 4.9$. In analogy to the nominal approach using the VELO-hit multiplicity, the same fractions of the full distribution are used to define relative activity classes for both beam configurations. Similarly, five common activity bins for the $p + \text{Pb}$ and $\text{Pb} + p$ samples are defined in the intermediate to high-activity classes. The results are found to be independent of the definition of the activity classes.

5. Analysis method

Two-particle correlations are measured separately for events in each activity class. The track sample containing the selected candidates of primary charged particles is divided into three p_T intervals: 0.15–1.0 GeV/c , 1.0–2.0 GeV/c and 2.0–3.0 GeV/c . For each event, all candidates within a given p_T interval are identified as *trigger* particles. By selecting a trigger particle all remaining candidates within the same interval compose the group of *associ-*

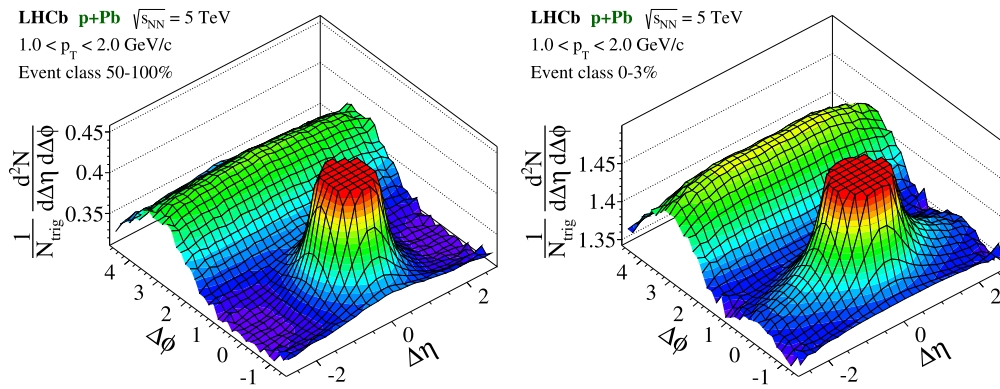


Fig. 2. Two-particle correlation functions for events recorded in the $p + \text{Pb}$ configuration, showing the (left) low and (right) high event-activity classes. The analysed pairs of prompt charged particles are selected in a p_T range of 1–2 GeV/c. The near-side peak around $\Delta\eta = \Delta\phi = 0$ is truncated in the histograms.

ated particles. Particle pairs are formed by combining every trigger particle with each associated particle. Due to the symmetry around the origin, differences in azimuthal angle $\Delta\phi$ are taken in the range $[0, \pi]$ and as absolute values in $\Delta\eta$. For visualisation purposes plots are symmetrized. The two-particle correlation function is composed of a signal part $S(\Delta\eta, \Delta\phi)$, a background part $B(\Delta\eta, \Delta\phi)$, and a normalization factor $B(0, 0)$. The total function is defined as the associated yield per trigger particle, given by

$$\frac{1}{N_{\text{trig}}} \frac{d^2 N_{\text{pair}}}{d\Delta\eta d\Delta\phi} = \frac{S(\Delta\eta, \Delta\phi)}{B(\Delta\eta, \Delta\phi)} \times B(0, 0), \quad (2)$$

where N_{pair} is the number of particle pairs found in a $(\Delta\eta, \Delta\phi)$ bin. The number of trigger particles within a given p_T interval and activity class is denoted by N_{trig} . The signal distribution $S(\Delta\eta, \Delta\phi)$ describes the associated yield per trigger particle for particle pairs, N_{same} , formed from the same event, and is defined as

$$S(\Delta\eta, \Delta\phi) = \frac{1}{N_{\text{trig}}} \frac{d^2 N_{\text{same}}}{d\Delta\eta d\Delta\phi}. \quad (3)$$

Following the approach in Ref. [6], the sum over the events is performed separately for N_{trig} and for $d^2 N_{\text{same}}/d\Delta\eta d\Delta\phi$ before the ratio is calculated. The background distribution $B(\Delta\eta, \Delta\phi)$ is defined for particle pairs of mixed events,

$$B(\Delta\eta, \Delta\phi) = \frac{d^2 N_{\text{mix}}}{d\Delta\eta d\Delta\phi}, \quad (4)$$

and describes the yield of uncorrelated particles. The N_{mix} pairs are constructed by combining all trigger particles of an event with the associated particles of five different random events in the same activity class, whose vertex positions in the beam direction are within 2 cm of the original event. As a result, effects due to the detector occupancy, acceptance and material are accounted for by dividing the signal by the background distribution, where the latter is normalised to unity around the origin. The factor $B(0, 0)$ describes the associated yield for particles of a pair travelling in approximately the same direction and thus having the maximum pair acceptance.

All trigger and associated particles in the signal and background distributions are weighted with the correction factors ω described in Section 3. Furthermore, alternative correction factors determined from the large pile-up pp simulation using PYTHIA are applied to evaluate systematic uncertainties. The resulting associated correlation yields agree within 3% with the nominal results. To estimate the influence of the track selection, the correction factors are also determined with a maximum impact parameter relaxed to twice the nominal value, and the value of the multivariate classifier used to suppress fake tracks is varied by $\pm 5\%$. The

resulting different correction factors are applied to the measurements which are then compared to the nominal corrected results. The difference due to the different prompt selection is negligible, while the alternative fake track suppression results in a maximum variation of 3%. Typical variations are much smaller. The effect on the final results, obtained after subtracting a global offset, is negligible.

6. Results

Two-particle correlation functions for events recorded in the $p + \text{Pb}$ configuration are presented in Fig. 2. The correlation for particles with $1 < p_T < 2$ GeV/c is shown for events of the 50–100% and 0–3% class, representing low and very-high event activities, respectively. Both histograms are dominated by the jet peak around $\Delta\eta \approx \Delta\phi \approx 0$ which is due to correlations of particles originating from the same jet-like objects and thus being boosted closely together. For better visualisation of additional structures, in all 2D-histograms the jet peak is truncated. The second prominent feature is visible on the away-side ($\Delta\phi \approx \pi$) over a long range in $\Delta\eta$ and combines jet and (potential) ridge contributions. The event sample with very high event activity (Fig. 2, right) shows an additional, less pronounced, long-range structure centred at $\Delta\phi = 0$, which is not present in the corresponding low-activity sample. The structure, often referred to as the near-side ridge, is elongated over the full measured $\Delta\eta$ range of 2.9 units. This observation of the ridge for particles produced in proton-lead collisions at forward rapidities, $2.0 < \eta < 4.9$, extends previous measurements at the LHC.

Two-particle correlations for events recorded in the $\text{Pb} + p$ configuration are shown in Fig. 3, for particle pairs with $1 < p_T < 2$ GeV/c. The 50–100% and 0–3% activity classes in the $\text{Pb} + p$ sample exhibit the same correlation structures as the corresponding classes in the $p + \text{Pb}$ sample. While the shape and magnitude of the jet peak and the away-side ridge appear to be of similar sizes in both beam configurations, the near-side ridge is more pronounced for particles in the direction of the lead beam. For the 3% of events with the highest event activity, the near-side ridge in the $\text{Pb} + p$ sample is much more prominent than that in the $p + \text{Pb}$ sample.

Similar behaviour is found when analysing particle pairs with larger transverse momenta in the interval $2 < p_T < 3$ GeV/c. In Fig. 4 the correlation functions in this p_T range are presented for the 3% highest-activity events recorded in the $p + \text{Pb}$ and $\text{Pb} + p$ configurations. The near-side ridge is present in both samples; however in the $p + \text{Pb}$ sample it is only marginally visible while in the $\text{Pb} + p$ sample a strongly pronounced ridge is found. The short-range jet peak in this higher p_T interval is more collimated compared to the 1–2 GeV/c interval, because of the higher average

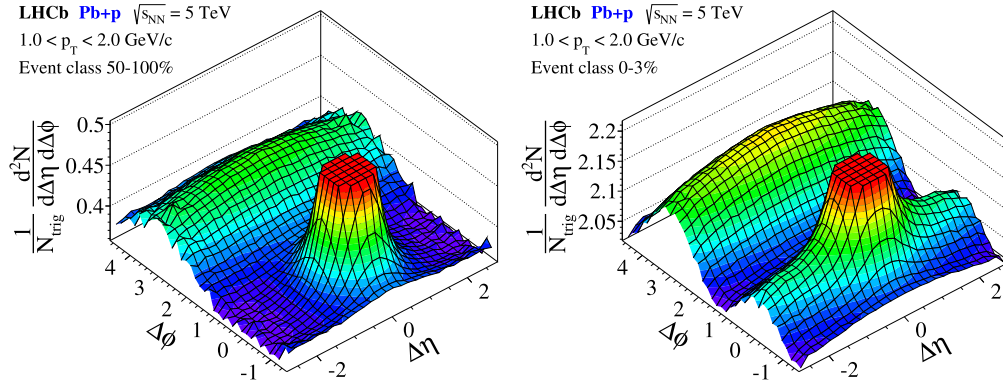


Fig. 3. Two-particle correlation functions for events recorded in the Pb + p configuration, showing the (left) low and (right) high event-activity classes. The analysed pairs of prompt charged particles are selected in a p_T range of 1–2 GeV/c. The near-side peak around $(\Delta\eta = \Delta\phi = 0)$ is truncated in the histograms.

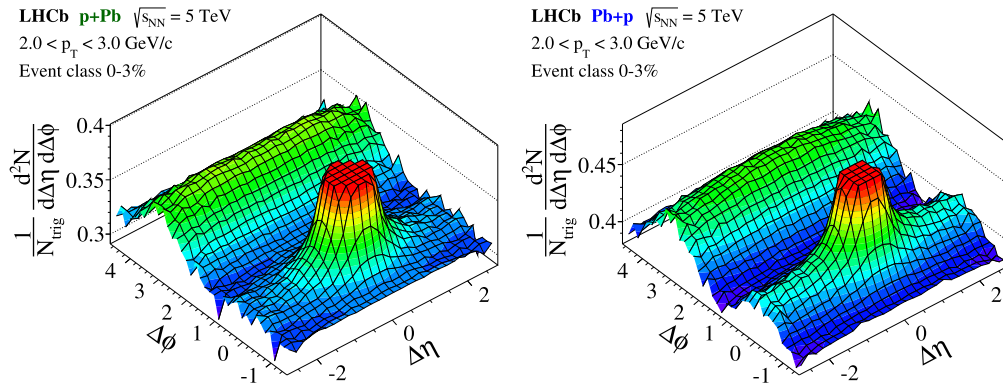


Fig. 4. Two-particle correlation functions for events recorded in the p + Pb (left) and Pb + p (right) configurations, showing the 0–3% event-activity class. The analysed pairs of prompt charged particles are selected in a p_T range of 2–3 GeV/c. The near-side peak around $(\Delta\eta = \Delta\phi = 0)$ is truncated in each histogram.

total momentum of the particles. As a result, the near-side ridge is visible towards $|\Delta\eta|$ values slightly below 2.0 without being covered by the jet peak.

In order to study the evolution of the long-range correlations on the near and away sides in more detail, one-dimensional projections of the correlation function on $\Delta\phi$ are calculated,

$$Y(\Delta\phi) \equiv \frac{1}{N_{\text{trig}}} \frac{dN_{\text{pair}}}{d\Delta\phi} = \frac{1}{\Delta\eta_b - \Delta\eta_a} \int_{\Delta\eta_a}^{\Delta\eta_b} \frac{1}{N_{\text{trig}}} \frac{d^2 N_{\text{pair}}}{d\Delta\eta d\Delta\phi} d\Delta\eta. \quad (5)$$

The short-range correlations, *e.g.* of the jet peak, are excluded by averaging the two-dimensional yield over the interval from $\Delta\eta_a = 2.0$ to $\Delta\eta_b = 2.9$. Since random particle combinations produce a flat pedestal in the yield, the correlation structures of interest are extracted by using the zero-yield-at-minimum (ZYAM) method [33,34]. By fitting a second-order polynomial to $Y(\Delta\phi)$ in the range $0.1 < \Delta\phi < 2.0$, the offset is estimated as the minimum of the polynomial. This value, further denoted as C_{ZYAM} , is subtracted from $Y(\Delta\phi)$ to shift its minimum to be at zero yield. The uncertainties on C_{ZYAM} due to the limited sample size and the fit range are below 0.002 for all individual measurements.

The subtracted one-dimensional yields for the p + Pb (full circles) and Pb + p (open circles) data samples are shown in Fig. 5 for all activity classes and p_T intervals. The correlation increases with event activity, but decreases towards higher p_T where fewer particles are found. Since more particles are emitted into the acceptance of the detector in the Pb + p compared to the p + Pb configuration, a larger offset is observed, as indicated by the ZYAM

constants. All distributions in Fig. 5 show a maximum at $\Delta\phi = \pi$, marking the centre of the away-side ridge, which balances the momentum of the near-side (the jet peak is excluded in this representation). The lower activity classes, 50–100% and 30–50%, do not have a corresponding maximum at $\Delta\phi = 0$. The 30–50% event class of the Pb + p sample shows a first change in shape of the distribution at $\Delta\phi = 0$. The picture changes when probing the intermediate activity class 10–30%. In all p_T intervals of the Pb + p sample the emergence of the near-side ridge with a second maximum at $\Delta\phi = 0$ is clearly visible. In the p + Pb sample the event activity is still not high enough to form a clear near-side structure. In the high-activity classes, 0–10% and 0–3%, the near-side ridge is strongly pronounced in the Pb + p sample in all p_T intervals. In the p + Pb sample the near-side structure is less distinct; however the $1 < p_T < 2$ GeV/c interval shows a clear near-side ridge.

A qualitatively similar behaviour is seen in the forward-central correlations studied by the ALICE experiment [9], with a forward muon trigger and central associated particles. Here also a clear ridge effect is observed, which grows with increasing event activity, and indications are seen that it is more pronounced in the hemisphere of the Pb nucleus.

Comparison of the ZYAM-subtracted yields shows that the away-side ridge is always more prominent than the near-side ridge. The ridge on the away-side is only weakly dependent on p_T , while the near-side ridge appears most pronounced in the bin $1 < p_T < 2$ GeV/c. Comparing p + Pb and Pb + p, one finds that especially for high event activities the near-side ridge is more pronounced in the Pb hemisphere.

Study of the one-dimensional yields within a p_T interval for different activity classes shows that the away side remains ap-

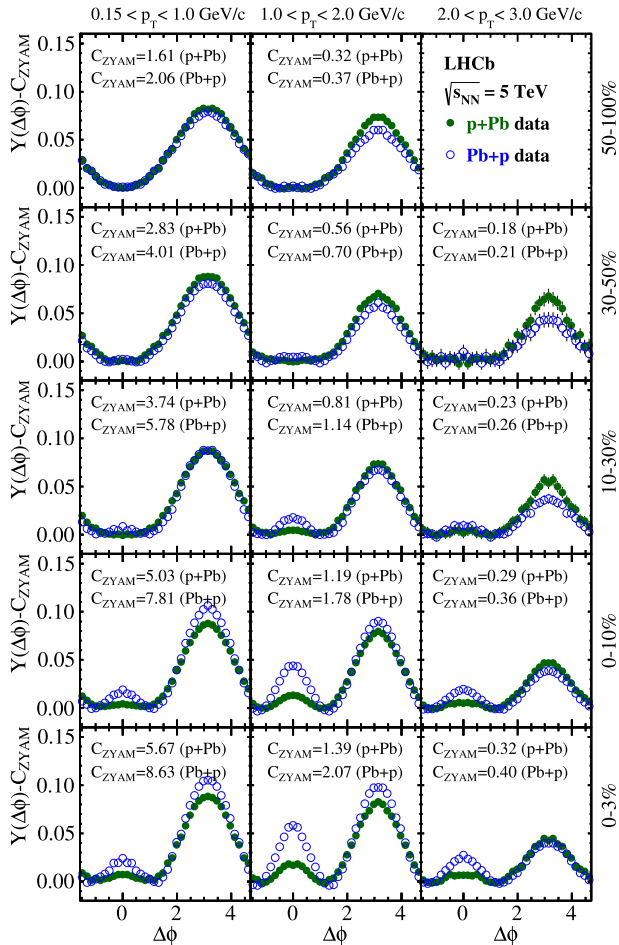


Fig. 5. One-dimensional correlation yield as a function of $\Delta\phi$ obtained from the ZYAM-method by averaging over $2.0 < \Delta\eta < 2.9$. The subtracted yields are presented for $\sqrt{s_{NN}} = 5$ TeV proton-lead collisions recorded in $p + \text{Pb}$ (full green circles) and $\text{Pb} + p$ (open blue circles) configurations. The ZYAM constant is given in each panel. Event classes are compared for low to very-high activities from top to bottom, and different intervals of increasing p_T from left to right. Only statistical uncertainties are shown. Error bars are often smaller than the markers. (For interpretation of the references to colour in this figure legend, the reader is referred to the web version of this article.)

proximately unchanged, while the near side starts to form the additional ridge when a certain event activity is reached. This turn-on, however, appears to be at different activities in the $p + \text{Pb}$ and $\text{Pb} + p$ configurations.

The same qualitative observations in the various analysis bins, including the emergence of the near-side ridge, are found when using the track-based approach for the definition of the activity classes as a systematic check. The total correlation yield varies by only a few percent, and the maximum variation does not exceed 10% in the low- p_T range. The emergence of the near-side ridge in the ZYAM-subtracted yield is unaffected by the change of the event activity definition.

Further systematic effects related to the event selection are evaluated by including events with multiple reconstructed primary vertices. The change of the final correlation yield is negligible. As another cross-check, data recorded in magnet up and down polarities are analysed separately. The results are in good agreement with each other.

To investigate the activity dependence of the long-range correlations in the $p + \text{Pb}$ and $\text{Pb} + p$ samples in more detail, common bins in absolute activity for both samples are studied. For this

purpose, events of both samples are probed in which a similar number of charged particles are emitted into the forward direction. Events of both samples are grouped into five narrow activity bins, as defined in Table 2. Fig. 6 compares the ZYAM-subtracted two-particle correlation yields in the range $1 < p_T < 2$ GeV/c, in which the near-side ridge is most pronounced. The uncertainty bands represent the systematic uncertainty on the scaling factor, which translates the activity of the $p + \text{Pb}$ configuration to that of the $\text{Pb} + p$ configuration. For $p + \text{Pb}$ and $\text{Pb} + p$ events of the same activity in the forward region, the observed long-range correlations become compatible within the uncertainties, except for bin I in which the away-side yield in $p + \text{Pb}$ is still slightly more pronounced. The near-side correlation in the beam (p) and target (Pb) fragmentation hemispheres shows a consistent increase with increasing event activity.

7. Summary and conclusions

Two-particle angular correlations between prompt charged particles produced in $p\text{Pb}$ collisions at $\sqrt{s_{NN}} = 5$ TeV have been measured for the first time in the forward region, using the LHCb detector. The angular correlations are studied in the laboratory frame in the pseudorapidity range $2.0 < \eta < 4.9$ over the full range of azimuthal angles, probing particle pairs in different common p_T intervals. With the asymmetric detector layout, the analysis is performed separately for the $p + \text{Pb}$ and $\text{Pb} + p$ beam configurations, which probe rapidities in the nucleon-nucleon centre-of-mass frame of $1.5 < y < 4.4$ and $-5.4 < y < -2.5$, respectively. The strength of the near-side ridge observed in the backward ($\text{Pb} + p$ configuration) region appears to be of similar size to that found in the forward ($p + \text{Pb}$ configuration) region. The relative shift of about one unit in nucleon-nucleon centre-of-mass rapidity between the two configurations produces no sizeable effect on the near-side ridge within the accuracy of the measurement. For events with high event activity a long-range correlation on the near side (the ridge) is observed in both configurations. While the correlation structure on the away side shrinks with increasing p_T , the near-side ridge is most pronounced in the range $1 < p_T < 2$ GeV/c. The observation of the ridge in the forward region extends previous LHC measurements, which show similar qualitative features. Furthermore, the correlation dependence on the event activity is investigated for relative and absolute activity ranges. The correlation structures on the near side and on the away side both grow stronger with increasing event activity. For identical absolute activity ranges in the $p + \text{Pb}$ and $\text{Pb} + p$ configurations the observed long-range correlations are compatible with each other.

Acknowledgements

We express our gratitude to our colleagues in the CERN accelerator departments for the excellent performance of the LHC. We thank the technical and administrative staff at the LHCb institutes. We acknowledge support from CERN and from the national agencies: CAPES, CNPq, FAPERJ and FINEP (Brazil); NSFC (China); CNRS/IN2P3 (France); BMBF, DFG and MPG (Germany); INFN (Italy); FOM and NWO (The Netherlands); MNIISW and NCN (Poland); MEN/IFA (Romania); MinES and FANO (Russia); MINECO (Spain); SNSF and SER (Switzerland); NASU (Ukraine); STFC (United Kingdom); NSF (USA). We acknowledge the computing resources that are provided by CERN, IN2P3 (France), KIT and DESY (Germany), INFN (Italy), SURF (The Netherlands), PIC (Spain), GridPP (United Kingdom), RRCKI (Russia), CSCS (Switzerland), IFIN-HH (Romania), CBPF (Brazil), PL-GRID (Poland) and OSC (USA). We are indebted to the communities behind the multiple open source

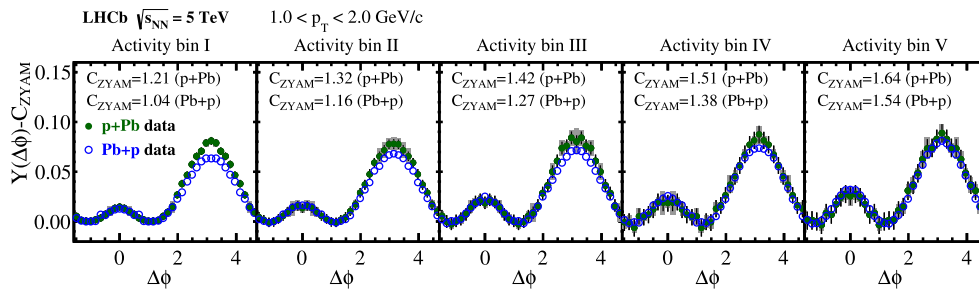


Fig. 6. One-dimensional correlation yield as a function of $\Delta\phi$ obtained from the ZYAM-method by averaging the two-dimensional distribution over $2.0 < \Delta\eta < 2.9$. The results for the $p + \text{Pb}$ and $\text{Pb} + p$ samples are compared in five event classes which probe identical activities in the range $2.0 < \eta < 4.9$. The measured hit-multiplicities of the $p + \text{Pb}$ sample are scaled to agree with the hit-multiplicities of the $\text{Pb} + p$ sample. The uncertainty band represents the systematic limitation of the scaling procedure. The error bars represent the statistical uncertainty. (For interpretation of the references to colour in this figure legend, the reader is referred to the web version of this article.)

software packages on which we depend. We are also thankful for the computing resources and the access to software R&D tools provided by Yandex LLC (Russia). Individual groups or members have received support from AvH Foundation (Germany), EPLANET, Marie Skłodowska-Curie Actions and ERC (European Union), Conseil Général de Haute-Savoie, Labex ENIGMASS and OCEVU, Région Auvergne (France), RFBR (Russia), GVA, XuntaGal and GENCAT (Spain), The Royal Society and Royal Commission for the Exhibition of 1851 (United Kingdom).

References

- [1] J.-Y. Ollitrault, Anisotropy as a signature of transverse collective flow, *Phys. Rev. D* 46 (1992) 229.
- [2] CMS Collaboration, V. Khachatryan, et al., Observation of long-range near-side angular correlations in proton–proton collisions at the LHC, *J. High Energy Phys.* 1009 (2010) 091, arXiv:1009.4122.
- [3] ATLAS Collaboration, G. Aad, et al., Observation of long-range elliptic azimuthal anisotropies in $\sqrt{s} = 13$ and 2.76 TeV pp collisions with the ATLAS detector, *Phys. Rev. Lett.* 116 (17) (2016) 172301, arXiv:1509.04776.
- [4] CMS Collaboration, V. Khachatryan, et al., Measurement of long-range near-side two-particle angular correlations in pp collisions at $\sqrt{s} = 13$ TeV, *Phys. Rev. Lett.* 116 (17) (2016) 172302, arXiv:1510.03068.
- [5] CMS Collaboration, S. Chatrchyan, et al., Observation of long-range near-side angular correlations in proton–lead collisions at the LHC, *Phys. Lett. B* 718 (2013) 795, arXiv:1210.5482.
- [6] ALICE Collaboration, B. Abelev, et al., Long-range angular correlations on the near and away side in p -Pb collisions at $\sqrt{s_{NN}} = 5.02$ TeV, *Phys. Lett. B* 719 (2013) 29, arXiv:1212.2001.
- [7] ATLAS Collaboration, G. Aad, et al., Observation of associated near-side and away-side long-range correlations in $\sqrt{s_{NN}} = 5.02$ TeV proton–lead collisions with the ATLAS detector, *Phys. Rev. Lett.* 110 (2013) 182302, arXiv:1212.5198.
- [8] ATLAS Collaboration, G. Aad, et al., Measurement of long-range pseudorapidity correlations and azimuthal harmonics in $\sqrt{s_{NN}} = 5.02$ TeV proton–lead collisions with the ATLAS detector, *Phys. Rev. C* 90 (2014) 044906, arXiv:1409.1792.
- [9] ALICE Collaboration, J. Adam, et al., Forward-central two-particle correlations in p -Pb collisions at $\sqrt{s_{NN}} = 5.02$ TeV, *Phys. Lett. B* 753 (2016) 126, arXiv:1506.08032.
- [10] K. Dusling, R. Venugopalan, Evidence for BFKL and saturation dynamics from dihadron spectra at the LHC, *Phys. Rev. D* 87 (2013) 051502, arXiv:1210.3890.
- [11] K. Dusling, R. Venugopalan, Explanation of systematics of CMS p +Pb high multiplicity di-hadron data at $\sqrt{s_{NN}} = 5.02$ TeV, *Phys. Rev. D* 87 (2013) 054014, arXiv:1211.3701.
- [12] K. Dusling, R. Venugopalan, Comparison of the color glass condensate to di-hadron correlations in proton–proton and proton–nucleus collisions, *Phys. Rev. D* 87 (2013) 094034, arXiv:1302.7018.
- [13] Y.V. Kovchegov, D.E. Wertepny, Long-range rapidity correlations in heavy-light ion collisions, *Nucl. Phys. A* 906 (2013) 50, arXiv:1212.1195.
- [14] A. Bzdak, B. Schenke, P. Tribedy, R. Venugopalan, Initial state geometry and the role of hydrodynamics in proton–proton, proton–nucleus and deuteron–nucleus collisions, *Phys. Rev. C* 87 (2013) 064906, arXiv:1304.3403.
- [15] S. Alderweireldt, P. Van Mechelen, Obtaining the CMS ridge effect with multiparton interactions, in: Proceedings of the 3rd International Workshop on Multiple Partonic Interactions at the LHC (MPI@LHC 2011), 2012, p. 33, arXiv:1203.2048.
- [16] M. Strikman, Transverse nucleon structure and multiparton interactions, *Acta Phys. Pol. B* 42 (2011) 2607, arXiv:1112.3834.
- [17] M.G. Ryskin, A.D. Martin, V.A. Khoze, Probes of multiparticle production at the LHC, *J. Phys. G* 38 (2011) 085006, arXiv:1105.4987.
- [18] R.C. Hwa, C.B. Yang, Ridge formation induced by jets in pp collisions at 7 TeV, *Phys. Rev. C* 83 (2011) 024911, arXiv:1011.0965.
- [19] C.-Y. Wong, Momentum Kick Model description of the ridge in $\Delta\phi$ - $\Delta\eta$ correlation in pp collisions at 7 TeV, *Phys. Rev. C* 84 (2011) 024901, arXiv:1105.5871.
- [20] E. Avsar, et al., Eccentricity and elliptic flow in proton–proton collisions from parton evolution, *Phys. Lett. B* 702 (2011) 394, arXiv:1009.5643.
- [21] K. Werner, I. Karpenko, T. Pierog, The ‘ridge’ in proton–proton scattering at 7 TeV, *Phys. Rev. Lett.* 106 (2011) 122004, arXiv:1011.0375.
- [22] P. Bozek, Collective flow in p -Pb and d -Pd collisions at TeV energies, *Phys. Rev. C* 85 (2012) 014911, arXiv:1112.0915.
- [23] P. Bozek, W. Broniowski, Correlations from hydrodynamic flow in p -Pb collisions, *Phys. Lett. B* 718 (2013) 1557, arXiv:1211.0845.
- [24] E. Shuryak, I. Zahed, High-multiplicity pp and pA collisions: hydrodynamics at its edge, *Phys. Rev. C* 88 (2013) 044915, arXiv:1301.4470.
- [25] LHCb Collaboration, A.A. Alves Jr., et al., The LHCb detector at the LHC, *J. Instrum.* 3 (2008) S08005.
- [26] LHCb Collaboration, R. Aaij, et al., LHCb detector performance, *Int. J. Mod. Phys. A* 30 (2015) 1530022, arXiv:1412.6352.
- [27] X.-N. Wang, M. Gyulassy, HIJING: a Monte Carlo model for multiple jet production in pp , pA and AA collisions, *Phys. Rev. D* 44 (1991) 3501.
- [28] T. Sjöstrand, S. Mrenna, P. Skands, A brief introduction to PYTHIA 8.1, *Comput. Phys. Commun.* 178 (2008) 852, arXiv:0710.3820; T. Sjöstrand, S. Mrenna, P. Skands, PYTHIA 6.4 physics and manual, *J. High Energy Phys.* 05 (2006) 026, arXiv:hep-ph/0603175.
- [29] I. Belyaev, et al., Handling of the generation of primary events in Gauss, the LHCb simulation framework, *J. Phys. Conf. Ser.* 331 (2011) 032047.
- [30] D.J. Lange, The EvtGen particle decay simulation package, *Nucl. Instrum. Methods A* 462 (2001) 152.
- [31] Geant4 Collaboration, J. Allison, et al., Geant4 developments and applications, *IEEE Trans. Nucl. Sci.* 53 (2006) 270; Geant4 Collaboration, S. Agostinelli, et al., Geant4: a simulation toolkit, *Nucl. Instrum. Methods* 506 (2003) 250.
- [32] M. Clemencic, et al., The LHCb simulation application, Gauss: design, evolution and experience, *J. Phys. Conf. Ser.* 331 (2011) 032023.
- [33] STAR Collaboration, C. Adler, et al., Disappearance of back-to-back high p_T hadron correlations in central Au + Au collisions at $\sqrt{s_{NN}} = 200$ GeV, *Phys. Rev. Lett.* 90 (2003) 082302, arXiv:nucl-ex/0210033.
- [34] N.N. Ajitanand, et al., Decomposition of harmonic and jet contributions to particle–pair correlations at ultrarelativistic energies, *Phys. Rev. C* 72 (2005) 011902.

LHCb Collaboration

R. Aaij³⁹, C. Abellán Beteta⁴¹, B. Adeva³⁸, M. Adinolfi⁴⁷, A. Affolder⁵³, Z. Ajaltouni⁵, S. Akar⁶, J. Albrecht¹⁰, F. Alessio³⁹, M. Alexander⁵², S. Ali⁴², G. Alkhazov³¹, P. Alvarez Cartelle⁵⁴, A.A. Alves Jr⁵⁸,

S. Amato², S. Amerio²³, Y. Amhis⁷, L. An³, L. Anderlini¹⁸, J. Anderson⁴¹, G. Andreassi⁴⁰,
 M. Andreotti^{17,f}, J.E. Andrews⁵⁹, R.B. Appleby⁵⁵, O. Aquines Gutierrez¹¹, F. Archilli³⁹, P. d'Argent¹²,
 A. Artamonov³⁶, M. Artuso⁶⁰, E. Aslanides⁶, G. Auriemma^{26,m}, M. Baalouch⁵, S. Bachmann¹²,
 J.J. Back⁴⁹, A. Badalov³⁷, C. Baesso⁶¹, W. Baldini^{17,39}, R.J. Barlow⁵⁵, C. Barschel³⁹, S. Barsuk⁷,
 W. Barter³⁹, V. Batozskaya²⁹, V. Battista⁴⁰, A. Bay⁴⁰, L. Beaucourt⁴, J. Beddow⁵², F. Bedeschi²⁴,
 I. Bediaga¹, L.J. Bel⁴², V. Bellee⁴⁰, N. Belloli^{21,j}, I. Belyaev³², E. Ben-Haim⁸, G. Bencivenni¹⁹,
 S. Benson³⁹, J. Benton⁴⁷, A. Berezhnoy³³, R. Bernet⁴¹, A. Bertolin²³, M.-O. Bettler³⁹,
 M. van Beuzekom⁴², A. Bien¹², S. Bifani⁴⁶, P. Billoir⁸, T. Bird⁵⁵, A. Birnkraut¹⁰, A. Bizzeti^{18,h},
 T. Blake⁴⁹, F. Blanc⁴⁰, J. Blouw¹¹, S. Blusk⁶⁰, V. Bocci²⁶, A. Bondar³⁵, N. Bondar^{31,39}, W. Bonivento¹⁶,
 S. Borghi⁵⁵, M. Borsato⁷, T.J.V. Bowcock⁵³, E. Bowen⁴¹, C. Bozzi¹⁷, S. Braun¹², M. Britsch¹¹,
 T. Britton⁶⁰, J. Brodzicka⁵⁵, N.H. Brook⁴⁷, E. Buchanan⁴⁷, C. Burr⁵⁵, A. Bursche⁴¹, J. Buytaert³⁹,
 S. Cadeddu¹⁶, R. Calabrese^{17,f}, M. Calvi^{21,j}, M. Calvo Gomez^{37,o}, P. Campana¹⁹, D. Campora Perez³⁹,
 L. Capriotti⁵⁵, A. Carbone^{15,d}, G. Carboni^{25,k}, R. Cardinale^{20,i}, A. Cardini¹⁶, P. Carniti^{21,j}, L. Carson⁵¹,
 K. Carvalho Akiba^{2,39}, G. Casse⁵³, L. Cassina^{21,j}, L. Castillo Garcia⁴⁰, M. Cattaneo³⁹, Ch. Cauet¹⁰,
 G. Cavallero²⁰, R. Cenci^{24,s}, M. Charles⁸, Ph. Charpentier³⁹, M. Chefdeville⁴, S. Chen⁵⁵, S.-F. Cheung⁵⁶,
 N. Chiapolini⁴¹, M. Chrzaszcz⁴¹, X. Cid Vidal³⁹, G. Ciezarek⁴², P.E.L. Clarke⁵¹, M. Clemencic³⁹,
 H.V. Cliff⁴⁸, J. Closier³⁹, V. Coco³⁹, J. Cogan⁶, E. Cogneras⁵, V. Cogoni^{16,e}, L. Cojocariu³⁰,
 G. Collazuol^{23,q}, P. Collins³⁹, A. Comerma-Montells¹², A. Contu¹⁶, A. Cook⁴⁷, M. Coombes⁴⁷,
 S. Coquereau⁸, G. Corti³⁹, M. Corvo^{17,f}, B. Couturier³⁹, G.A. Cowan⁵¹, D.C. Craik⁴⁹, A. Crocombe⁴⁹,
 M. Cruz Torres⁶¹, S. Cunliffe⁵⁴, R. Currie⁵⁴, C. D'Ambrosio³⁹, E. Dall'Occo⁴², J. Dalseno⁴⁷, P.N.Y. David⁴²,
 A. Davis⁵⁸, O. De Aguiar Francisco², K. De Bruyn⁶, S. De Capua⁵⁵, M. De Cian¹², J.M. De Miranda¹,
 L. De Paula², P. De Simone¹⁹, C.-T. Dean⁵², D. Decamp⁴, M. Deckenhoff¹⁰, L. Del Buono⁸, N. Déleage⁴,
 M. Demmer¹⁰, D. Derkach⁶⁶, O. Deschamps⁵, F. Dettori³⁹, B. Dey²², A. Di Canto³⁹, F. Di Ruscio²⁵,
 H. Dijkstra³⁹, S. Donleavy⁵³, F. Dordei¹², M. Dorigo⁴⁰, A. Dosil Suárez³⁸, D. Dossett⁴⁹, A. Dovbnya⁴⁴,
 K. Dreimann⁵³, L. Dufour⁴², G. Dujany⁵⁵, F. Dupertuis⁴⁰, P. Durante³⁹, R. Dzhelyadin³⁶, A. Dziurda²⁷,
 A. Dzyuba³¹, S. Easo^{50,39}, U. Egede⁵⁴, V. Egorychev³², S. Eidelman³⁵, S. Eisenhardt⁵¹, U. Eitschberger¹⁰,
 R. Ekelhof¹⁰, L. Eklund⁵², I. El Rifai⁵, Ch. Elsasser⁴¹, S. Ely⁶⁰, S. Esen¹², H.M. Evans⁴⁸, T. Evans⁵⁶,
 A. Falabella¹⁵, C. Färber³⁹, N. Farley⁴⁶, S. Farry⁵³, R. Fay⁵³, D. Ferguson⁵¹, V. Fernandez Albor³⁸,
 F. Ferrari¹⁵, F. Ferreira Rodrigues¹, M. Ferro-Luzzi³⁹, S. Filippov³⁴, M. Fiore^{17,39,f}, M. Fiorini^{17,f},
 M. Firlej²⁸, C. Fitzpatrick⁴⁰, T. Fiutowski²⁸, K. Fohl³⁹, P. Fol⁵⁴, M. Fontana¹⁶, F. Fontanelli^{20,i},
 D.C. Forshaw⁶⁰, R. Forty³⁹, M. Frank³⁹, C. Frei³⁹, M. Frosini¹⁸, J. Fu²², E. Furfaro^{25,k},
 A. Gallas Torreira³⁸, D. Galli^{15,d}, S. Gallorini²³, S. Gambetta⁵¹, M. Gandelman², P. Gandini⁵⁶, Y. Gao³,
 J. García Pardiñas³⁸, J. Garra Tico⁴⁸, L. Garrido³⁷, D. Gascon³⁷, C. Gaspar³⁹, R. Gauld⁵⁶, L. Gavardi¹⁰,
 G. Gazzoni⁵, D. Gerick¹², E. Gersabeck¹², M. Gersabeck⁵⁵, T. Gershon⁴⁹, Ph. Ghez⁴, S. Gianì⁴⁰,
 V. Gibson⁴⁸, O.G. Girard⁴⁰, L. Giubega³⁰, V.V. Gligorov³⁹, C. Göbel⁶¹, D. Golubkov³², A. Golutvin^{54,39},
 A. Gomes^{1,a}, C. Gotti^{21,j}, M. Grabalosa Gándara⁵, R. Graciani Diaz³⁷, L.A. Granado Cardoso³⁹,
 E. Graugés³⁷, E. Graverini⁴¹, G. Graziani¹⁸, A. Greco³⁰, E. Greening⁵⁶, S. Gregson⁴⁸, P. Griffith⁴⁶,
 L. Grillo¹², O. Grünberg⁶⁴, B. Gui⁶⁰, E. Gushchin³⁴, Yu. Guz^{36,39}, T. Gys³⁹, T. Hadavizadeh⁵⁶,
 C. Hadjivasiliou⁶⁰, G. Haefeli⁴⁰, C. Haen³⁹, S.C. Haines⁴⁸, S. Hall⁵⁴, B. Hamilton⁵⁹, X. Han¹²,
 S. Hansmann-Menzemer¹², N. Harnew⁵⁶, S.T. Harnew⁴⁷, J. Harrison⁵⁵, J. He³⁹, T. Head⁴⁰, V. Heijne⁴²,
 A. Heister⁹, K. Hennessy⁵³, P. Henrard⁵, L. Henry⁸, J.A. Hernando Morata³⁸, E. van Herwijnen³⁹,
 M. Heß⁶⁴, A. Hicheur², D. Hill⁵⁶, M. Hoballah⁵, C. Hombach⁵⁵, W. Hulsbergen⁴², T. Humair⁵⁴,
 N. Hussain⁵⁶, D. Hutchcroft⁵³, D. Hynds⁵², M. Idzik²⁸, P. Ilten⁵⁷, R. Jacobsson³⁹, A. Jaeger¹²,
 J. Jalocha⁵⁶, E. Jans⁴², A. Jawahery⁵⁹, F. Jing³, M. John⁵⁶, D. Johnson³⁹, C.R. Jones⁴⁸, C. Joram³⁹,
 B. Jost³⁹, N. Jurik⁶⁰, S. Kandybei⁴⁴, W. Kanso⁶, M. Karacson³⁹, T.M. Karbach^{39,†}, S. Karodia⁵²,
 M. Kecke¹², M. Kelsey⁶⁰, I.R. Kenyon⁴⁶, M. Kenzie³⁹, T. Ketel⁴³, E. Khairullin⁶⁶, B. Khanji^{21,39,j},
 C. Khurewathanakul⁴⁰, T. Kirn⁹, S. Klaver⁵⁵, K. Klimaszewski²⁹, O. Kochebina⁷, M. Kolpin¹²,
 I. Komarov⁴⁰, R.F. Koopman⁴³, P. Koppenburg^{42,39}, M. Kozeiha⁵, L. Kravchuk³⁴, K. Kreplin¹²,
 M. Kreps⁴⁹, G. Krocker¹², P. Krokovny³⁵, F. Kruse¹⁰, W. Krzemien²⁹, W. Kucewicz^{27,n}, M. Kucharczyk²⁷,
 V. Kudryavtsev³⁵, A.K. Kuonen⁴⁰, K. Kurek²⁹, T. Kvaratskheliya³², D. Lacarrere³⁹, G. Lafferty^{55,39},
 A. Lai¹⁶, D. Lambert⁵¹, G. Lanfranchi¹⁹, C. Langenbruch⁴⁹, B. Langhans³⁹, T. Latham⁴⁹, C. Lazzeroni⁴⁶,
 R. Le Gac⁶, J. van Leerdam⁴², J.-P. Lees⁴, R. Lefèvre⁵, A. Leflat^{33,39}, J. Lefrançois⁷, E. Lemos Cid³⁸,

O. Leroy⁶, T. Lesiak²⁷, B. Leverington¹², Y. Li⁷, T. Likhomanenko^{66,65}, M. Liles⁵³, R. Lindner³⁹, C. Linn³⁹, F. Lionetto⁴¹, B. Liu¹⁶, X. Liu³, D. Loh⁴⁹, I. Longstaff⁵², J.H. Lopes², D. Lucchesi^{23,q}, M. Lucio Martinez³⁸, H. Luo⁵¹, A. Lupato²³, E. Luppi^{17,f}, O. Lupton⁵⁶, A. Lusiani²⁴, F. Machefert⁷, F. Maciuc³⁰, O. Maev³¹, K. Maguire⁵⁵, S. Malde⁵⁶, A. Malinin⁶⁵, G. Manca⁷, G. Mancinelli⁶, P. Manning⁶⁰, A. Mapelli³⁹, J. Maratas⁵, J.F. Marchand⁴, U. Marconi¹⁵, C. Marin Benito³⁷, P. Marino^{24,39,s}, J. Marks¹², G. Martellotti²⁶, M. Martin⁶, M. Martinelli⁴⁰, D. Martinez Santos³⁸, F. Martinez Vidal⁶⁷, D. Martins Tostes², A. Massafferri¹, R. Matev³⁹, A. Mathad⁴⁹, Z. Mathe³⁹, C. Matteuzzi²¹, A. Mauri⁴¹, B. Maurin⁴⁰, A. Mazurov⁴⁶, M. McCann⁵⁴, J. McCarthy⁴⁶, A. McNab⁵⁵, R. McNulty¹³, B. Meadows⁵⁸, F. Meier¹⁰, M. Meissner¹², D. Melnychuk²⁹, M. Merk⁴², E. Michielin²³, D.A. Milanes⁶³, M.-N. Minard⁴, D.S. Mitzel¹², J. Molina Rodriguez⁶¹, I.A. Monroy⁶³, S. Monteil⁵, M. Morandin²³, P. Morawski²⁸, A. Mordà⁶, M.J. Morello^{24,s}, J. Moron²⁸, A.B. Morris⁵¹, R. Mountain⁶⁰, F. Muheim⁵¹, D. Müller⁵⁵, J. Müller¹⁰, K. Müller⁴¹, V. Müller¹⁰, M. Mussini¹⁵, B. Muster⁴⁰, P. Naik⁴⁷, T. Nakada⁴⁰, R. Nandakumar⁵⁰, A. Nandi⁵⁶, I. Nasteva², M. Needham⁵¹, N. Neri²², S. Neubert¹², N. Neufeld³⁹, M. Neuner¹², A.D. Nguyen⁴⁰, T.D. Nguyen⁴⁰, C. Nguyen-Mau^{40,p}, V. Niess⁵, R. Niet¹⁰, N. Nikitin³³, T. Nikodem¹², A. Novoselov³⁶, D.P. O'Hanlon⁴⁹, A. Oblakowska-Mucha²⁸, V. Obraztsov³⁶, S. Ogilvy⁵², O. Okhrimenko⁴⁵, R. Oldeman^{16,e}, C.J.G. Onderwater⁶⁸, B. Osorio Rodrigues¹, J.M. Otalora Goicochea², A. Otto³⁹, P. Owen⁵⁴, A. Oyanguren⁶⁷, A. Palano^{14,c}, F. Palombo^{22,t}, M. Palutan¹⁹, J. Panman³⁹, A. Papanestis⁵⁰, M. Pappagallo⁵², L.L. Pappalardo^{17,f}, C. Pappenheimer⁵⁸, W. Parker⁵⁹, C. Parkes⁵⁵, G. Passaleva¹⁸, G.D. Patel⁵³, M. Patel⁵⁴, C. Patrignani^{20,i}, A. Pearce^{55,50}, A. Pellegrino⁴², G. Penso^{26,l}, M. Pepe Altarelli³⁹, S. Perazzini^{15,d}, P. Perret⁵, L. Pescatore⁴⁶, K. Petridis⁴⁷, A. Petrolini^{20,i}, M. Petruzzo²², E. Picatoste Olloqui³⁷, B. Pietrzyk⁴, T. Pilař⁴⁹, D. Pinci²⁶, A. Pistone²⁰, A. Piucci¹², S. Playfer⁵¹, M. Plo Casasus³⁸, T. Poikela³⁹, F. Polci⁸, A. Poluektov^{49,35}, I. Polyakov³², E. Polcarpo², A. Popov³⁶, D. Popov^{11,39}, B. Popovici³⁰, C. Potterat², E. Price⁴⁷, J.D. Price⁵³, J. Prisciandaro³⁸, A. Pritchard⁵³, C. Prouve⁴⁷, V. Pugatch⁴⁵, A. Puig Navarro⁴⁰, G. Punzi^{24,r}, W. Qian⁴, R. Quagliani^{7,47}, B. Rachwal²⁷, J.H. Rademacker⁴⁷, M. Rama²⁴, M.S. Rangel², I. Raniuk⁴⁴, N. Rauschmayr³⁹, G. Raven⁴³, F. Redi⁵⁴, S. Reichert⁵⁵, M.M. Reid⁴⁹, A.C. dos Reis¹, S. Ricciardi⁵⁰, S. Richards⁴⁷, M. Rihl³⁹, K. Rinnert^{53,39}, V. Rives Molina³⁷, P. Robbe^{7,39}, A.B. Rodrigues¹, E. Rodrigues⁵⁵, J.A. Rodriguez Lopez⁶³, P. Rodriguez Perez⁵⁵, S. Roiser³⁹, V. Romanovsky³⁶, A. Romero Vidal³⁸, J.W. Ronayne¹³, M. Rotondo²³, J. Rouvinet⁴⁰, T. Ruf³⁹, P. Ruiz Valls⁶⁷, J.J. Saborido Silva³⁸, N. Sagidova³¹, P. Sail⁵², B. Saitta^{16,e}, V. Salustino Guimaraes², C. Sanchez Mayordomo⁶⁷, B. Sanmartin Sedes³⁸, R. Santacesaria²⁶, C. Santamarina Rios³⁸, M. Santimaria¹⁹, E. Santovetti^{25,k}, A. Sarti^{19,l}, C. Satriano^{26,m}, A. Satta²⁵, D.M. Saunders⁴⁷, D. Savrina^{32,33}, S. Schael⁹, M. Schiller³⁹, H. Schindler³⁹, M. Schlupp¹⁰, M. Schmelling¹¹, T. Schmelzer¹⁰, B. Schmidt³⁹, O. Schneider⁴⁰, A. Schopper³⁹, M. Schubiger⁴⁰, M.-H. Schune⁷, R. Schwemmer³⁹, B. Sciascia¹⁹, A. Sciubba^{26,l}, A. Semennikov³², A. Sergi⁴⁶, N. Serra⁴¹, J. Serrano⁶, L. Sestini²³, P. Seyfert²¹, M. Shapkin³⁶, I. Shapoval^{17,44,f}, Y. Shcheglov³¹, T. Shears⁵³, L. Shekhtman³⁵, V. Shevchenko⁶⁵, A. Shires¹⁰, B.G. Siddi¹⁷, R. Silva Coutinho⁴¹, L. Silva de Oliveira², G. Simi^{23,r}, M. Sirendi⁴⁸, N. Skidmore⁴⁷, T. Skwarnicki⁶⁰, E. Smith^{56,50}, E. Smith⁵⁴, I.T. Smith⁵¹, J. Smith⁴⁸, M. Smith⁵⁵, H. Snoek⁴², M.D. Sokoloff^{58,39}, F.J.P. Soler⁵², F. Soomro⁴⁰, D. Souza⁴⁷, B. Souza De Paula², B. Spaan¹⁰, P. Spradlin⁵², S. Sridharan³⁹, F. Stagni³⁹, M. Stahl¹², S. Stahl³⁹, S. Stefkova⁵⁴, O. Steinkamp⁴¹, O. Stenyakin³⁶, S. Stevenson⁵⁶, S. Stoica³⁰, S. Stone⁶⁰, B. Storaci⁴¹, S. Stracka^{24,s}, M. Straticiu³⁰, U. Straumann⁴¹, L. Sun⁵⁸, W. Sutcliffe⁵⁴, K. Swientek²⁸, S. Swientek¹⁰, V. Syropoulos⁴³, M. Szczekowski²⁹, T. Szumlak²⁸, S. T'Jampens⁴, A. Tayduganov⁶, T. Tekampe¹⁰, M. Teklishyn⁷, G. Tellarini^{17,f}, F. Teubert³⁹, C. Thomas⁵⁶, E. Thomas³⁹, J. van Tilburg⁴², V. Tisserand⁴, M. Tobin⁴⁰, J. Todd⁵⁸, S. Tolk⁴³, L. Tomassetti^{17,f}, D. Tonelli³⁹, S. Topp-Joergensen⁵⁶, N. Torr⁵⁶, E. Tournefier⁴, S. Tourneur⁴⁰, K. Trabelsi⁴⁰, M.T. Tran⁴⁰, M. Tresch⁴¹, A. Trisovic³⁹, A. Tsaregorodtsev⁶, P. Tsopelas⁴², N. Tuning^{42,39}, A. Ukleja²⁹, A. Ustyuzhanin^{66,65}, U. Uwer¹², C. Vacca^{16,39,e}, V. Vagnoni¹⁵, G. Valenti¹⁵, A. Vallier⁷, R. Vazquez Gomez¹⁹, P. Vazquez Regueiro³⁸, C. Vázquez Sierra³⁸, S. Vecchi¹⁷, M. van Veghel⁴³, J.J. Velthuis⁴⁷, M. Veltri^{18,g}, G. Veneziano⁴⁰, M. Vesterinen¹², B. Viaud⁷, D. Vieira², M. Vieites Diaz³⁸, X. Vilasis-Cardona^{37,o}, V. Volkov³³, A. Vollhardt⁴¹, D. Volynskyy¹¹, D. Voong⁴⁷, A. Vorobyev³¹, V. Vorobyev³⁵, C. Voß⁶⁴, J.A. de Vries⁴², R. Waldi⁶⁴, C. Wallace⁴⁹, R. Wallace¹³, J. Walsh²⁴, S. Wandernoth¹², J. Wang⁶⁰, D.R. Ward⁴⁸, N.K. Watson⁴⁶, D. Websdale⁵⁴, A. Weiden⁴¹,

M. Whitehead⁴⁹, G. Wilkinson^{56,39}, M. Wilkinson⁶⁰, M. Williams³⁹, M.P. Williams⁴⁶, M. Williams⁵⁷, T. Williams⁴⁶, F.F. Wilson⁵⁰, J. Wimberley⁵⁹, J. Wishahi¹⁰, W. Wislicki²⁹, M. Witek²⁷, G. Wormser⁷, S.A. Wotton⁴⁸, S. Wright⁴⁸, K. Wyllie³⁹, Y. Xie⁶², Z. Xu⁴⁰, Z. Yang³, J. Yu⁶², X. Yuan³⁵, O. Yushchenko³⁶, M. Zangoli¹⁵, M. Zavertyaev^{11,b}, L. Zhang³, Y. Zhang³, A. Zhelezov¹², A. Zhokhov³², L. Zhong³, V. Zhukov⁹, S. Zucchelli¹⁵

¹ Centro Brasileiro de Pesquisas Físicas (CBPF), Rio de Janeiro, Brazil

² Universidade Federal do Rio de Janeiro (UFRJ), Rio de Janeiro, Brazil

³ Center for High Energy Physics, Tsinghua University, Beijing, China

⁴ LAPP, Université Savoie Mont-Blanc, CNRS/IN2P3, Annecy-Le-Vieux, France

⁵ Clermont Université, Université Blaise Pascal, CNRS/IN2P3, LPC, Clermont-Ferrand, France

⁶ CPPM, Aix-Marseille Université, CNRS/IN2P3, Marseille, France

⁷ LAL, Université Paris-Sud, CNRS/IN2P3, Orsay, France

⁸ LPNHE, Université Pierre et Marie Curie, Université Paris Diderot, CNRS/IN2P3, Paris, France

⁹ I. Physikalisches Institut, RWTH Aachen University, Aachen, Germany

¹⁰ Fakultät Physik, Technische Universität Dortmund, Dortmund, Germany

¹¹ Max-Planck-Institut für Kernphysik (MPIK), Heidelberg, Germany

¹² Physikalisches Institut, Ruprecht-Karls-Universität Heidelberg, Heidelberg, Germany

¹³ School of Physics, University College Dublin, Dublin, Ireland

¹⁴ Sezione INFN di Bari, Bari, Italy

¹⁵ Sezione INFN di Bologna, Bologna, Italy

¹⁶ Sezione INFN di Cagliari, Cagliari, Italy

¹⁷ Sezione INFN di Ferrara, Ferrara, Italy

¹⁸ Sezione INFN di Firenze, Firenze, Italy

¹⁹ Laboratori Nazionali dell'INFN di Frascati, Frascati, Italy

²⁰ Sezione INFN di Genova, Genova, Italy

²¹ Sezione INFN di Milano Bicocca, Milano, Italy

²² Sezione INFN di Milano, Milano, Italy

²³ Sezione INFN di Padova, Padova, Italy

²⁴ Sezione INFN di Pisa, Pisa, Italy

²⁵ Sezione INFN di Roma Tor Vergata, Roma, Italy

²⁶ Sezione INFN di Roma La Sapienza, Roma, Italy

²⁷ Henryk Niewodniczanski Institute of Nuclear Physics, Polish Academy of Sciences, Kraków, Poland

²⁸ AGH – University of Science and Technology, Faculty of Physics and Applied Computer Science, Kraków, Poland

²⁹ National Center for Nuclear Research (NCBJ), Warsaw, Poland

³⁰ Horia Hulubei National Institute of Physics and Nuclear Engineering, Bucharest-Magurele, Romania

³¹ Petersburg Nuclear Physics Institute (PNPI), Gatchina, Russia

³² Institute of Theoretical and Experimental Physics (ITEP), Moscow, Russia

³³ Institute of Nuclear Physics, Moscow State University (SINP MSU), Moscow, Russia

³⁴ Institute for Nuclear Research of the Russian Academy of Sciences (INR RAN), Moscow, Russia

³⁵ Budker Institute of Nuclear Physics (SB RAS) and Novosibirsk State University, Novosibirsk, Russia

³⁶ Institute for High Energy Physics (IHEP), Protvino, Russia

³⁷ Universitat de Barcelona, Barcelona, Spain

³⁸ Universidad de Santiago de Compostela, Santiago de Compostela, Spain

³⁹ European Organization for Nuclear Research (CERN), Geneva, Switzerland

⁴⁰ Ecole Polytechnique Fédérale de Lausanne (EPFL), Lausanne, Switzerland

⁴¹ Physik-Institut, Universität Zürich, Zürich, Switzerland

⁴² Nikhef National Institute for Subatomic Physics, Amsterdam, The Netherlands

⁴³ Nikhef National Institute for Subatomic Physics and VU University Amsterdam, Amsterdam, The Netherlands

⁴⁴ NSC Kharkiv Institute of Physics and Technology (NSC KIPT), Kharkiv, Ukraine

⁴⁵ Institute for Nuclear Research of the National Academy of Sciences (KINR), Kyiv, Ukraine

⁴⁶ University of Birmingham, Birmingham, United Kingdom

⁴⁷ H.H. Wills Physics Laboratory, University of Bristol, Bristol, United Kingdom

⁴⁸ Cavendish Laboratory, University of Cambridge, Cambridge, United Kingdom

⁴⁹ Department of Physics, University of Warwick, Coventry, United Kingdom

⁵⁰ STFC Rutherford Appleton Laboratory, Didcot, United Kingdom

⁵¹ School of Physics and Astronomy, University of Edinburgh, Edinburgh, United Kingdom

⁵² School of Physics and Astronomy, University of Glasgow, Glasgow, United Kingdom

⁵³ Oliver Lodge Laboratory, University of Liverpool, Liverpool, United Kingdom

⁵⁴ Imperial College London, London, United Kingdom

⁵⁵ School of Physics and Astronomy, University of Manchester, Manchester, United Kingdom

⁵⁶ Department of Physics, University of Oxford, Oxford, United Kingdom

⁵⁷ Massachusetts Institute of Technology, Cambridge, MA, United States

⁵⁸ University of Cincinnati, Cincinnati, OH, United States

⁵⁹ University of Maryland, College Park, MD, United States

⁶⁰ Syracuse University, Syracuse, NY, United States

⁶¹ Pontifícia Universidade Católica do Rio de Janeiro (PUC-Rio), Rio de Janeiro, Brazil^u

⁶² Institute of Particle Physics, Central China Normal University, Wuhan, Hubei, China^v

⁶³ Departamento de Física, Universidad Nacional de Colombia, Bogota, Colombia^w

⁶⁴ Institut für Physik, Universität Rostock, Rostock, Germany^x

⁶⁵ National Research Centre Kurchatov Institute, Moscow, Russia^y

⁶⁶ Yandex School of Data Analysis, Moscow, Russia^y

⁶⁷ Instituto de Física Corpuscular (IFIC), Universitat de Valencia-CSIC, Valencia, Spain^z

⁶⁸ Van Swinderen Institute, University of Groningen, Groningen, The Netherlands^{aa}

- ^a Universidade Federal do Triângulo Mineiro (UFTM), Uberaba-MG, Brazil.
- ^b P.N. Lebedev Physical Institute, Russian Academy of Science (LPI RAS), Moscow, Russia.
- ^c Università di Bari, Bari, Italy.
- ^d Università di Bologna, Bologna, Italy.
- ^e Università di Cagliari, Cagliari, Italy.
- ^f Università di Ferrara, Ferrara, Italy.
- ^g Università di Urbino, Urbino, Italy.
- ^h Università di Modena e Reggio Emilia, Modena, Italy.
- ⁱ Università di Genova, Genova, Italy.
- ^j Università di Milano Bicocca, Milano, Italy.
- ^k Università di Roma Tor Vergata, Roma, Italy.
- ^l Università di Roma La Sapienza, Roma, Italy.
- ^m Università della Basilicata, Potenza, Italy.
- ⁿ AGH – University of Science and Technology, Faculty of Computer Science, Electronics and Telecommunications, Kraków, Poland.
- ^o LIFAELS, La Salle, Universitat Ramon Llull, Barcelona, Spain.
- ^p Hanoi University of Science, Hanoi, Viet Nam.
- ^q Università di Padova, Padova, Italy.
- ^r Università di Pisa, Pisa, Italy.
- ^s Scuola Normale Superiore, Pisa, Italy.
- ^t Università degli Studi di Milano, Milano, Italy.
- ^u Associated to Universidade Federal do Rio de Janeiro (UFRJ), Rio de Janeiro, Brazil.
- ^v Associated to Center for High Energy Physics, Tsinghua University, Beijing, China.
- ^w Associated to LPNHE, Université Pierre et Marie Curie, Université Paris Diderot, CNRS/IN2P3, Paris, France.
- ^x Associated to Physikalisches Institut, Ruprecht-Karls-Universität Heidelberg, Heidelberg, Germany.
- ^y Associated to Institute of Theoretical and Experimental Physics (ITEP), Moscow, Russia.
- ^z Associated to Universitat de Barcelona, Barcelona, Spain.
- ^{aa} Associated to Nikhef National Institute for Subatomic Physics, Amsterdam, The Netherlands.
- [†] Deceased.